





RESEARCH ARTICLE | SEPTEMBER 08 2023

Spray combustion characteristics of a gas–liquid pintle injector with variable swirl intensities

Chengming He (何成明) ; Weihang Luo (罗苇航) ; Peng Zhang (张鹏) ; Zhixia He (何志霞) ; Lianjie Yue (岳连捷)  



Physics of Fluids 35, 097111 (2023)

<https://doi.org/10.1063/5.0164130>



View
Online



Export
Citation

Physics of Fluids

Special Topic:

John Michael Dealy (1937-2024): Celebrating His Life

Guest Editors: Alan Jeffrey Giacomini and Savvas G. Hatzikiriakos

[Submit Today!](#)

Spray combustion characteristics of a gas-liquid pintle injector with variable swirl intensities

Cite as: Phys. Fluids **35**, 097111 (2023); doi: 10.1063/5.0164130

Submitted: 21 June 2023 · Accepted: 17 August 2023 ·

Published Online: 8 September 2023



View Online



Export Citation



CrossMark

Chengming He (何成明),^{1,2} Weihang Luo (罗苇航),² Peng Zhang (张鹏),³ Zhixia He (何志霞),¹
and Lianjie Yue (岳连捷)^{2,4,a)}

AFFILIATIONS

¹Institute for Energy Research, Jiangsu University, Zhenjiang 212013, China

²State Key Laboratory of High Temperature Gas Dynamics, Institute of Mechanics, Chinese Academy of Sciences, Beijing 100190, China

³Department of Mechanical Engineering, City University of Hong Kong, Kowloon Tong, Kowloon 999077, Hong Kong

⁴School of Engineering Science, University of Chinese Academy of Sciences, Beijing 100049, China

^{a)} Author to whom correspondence should be addressed: yuelj@imech.ac.cn

ABSTRACT

The present paper experimentally verified and computationally explained an improved design concept of the spray combustion of a gas-liquid pintle injector with variable swirl intensities. By pintle injector, we mean a promising injector for the throttleable engines with variable thrust capacities, which features the moveable pintle continuously controlling the mass flow rates of fuel and oxidizer where the radial and axial flows encounter to form a spray cone and spray atomization. First, the cold flow test was conducted to study the swirl effects on the spray angle, followed by the combustion test to study the total pressure and the specific impulse under different swirl intensities. The results show that the swirl enhances the combustion performance by increasing the total pressure and specific impulse. Second, the swirl-assisted spray was numerically simulated based on a validated volume-of-fluid method to explain the experimental findings. The diameter distribution and spatial distribution of dispersed droplets were analyzed by the Sauter mean diameter (SMD) and the Voronoi tessellation, respectively. The results show that the swirl significantly promotes the breakup of liquid jet or film, producing smaller SMDs and a more uniform spatial distribution of dispersed droplets. The consolidated correlation between the non-reacting spray characteristics and the combustion performance suggests that the proposed methodology can be used to fast prescreen pintle injector designs.

Published under an exclusive license by AIP Publishing. <https://doi.org/10.1063/5.0164130>

I. INTRODUCTION

Pintle injection strategy is admitted as one of the best choices for throttleable rocket engines^{1–3} among various strategies to adjust the mass flow rate, such as adjusting upstream injection pressure drop, inserting inactive gas into the fuel before injection, multiple manifolds,⁴ and high-speed pulse injection. The variable thrust capacity is promising and superior for wide-range flight vehicles^{5,6} and hypersonic aircrafts⁷ to improve maneuverability. Generally, pintle injection has two representative types, namely, gas-liquid and liquid-liquid injection forms. The cryogenic fuels, such as liquid oxygen/kerosene⁸ and liquid oxygen/methane,⁹ or gelled hypergolic propellants¹⁰ adopt the liquid-liquid injection form; and other fuels, such as hydrogen peroxide/kerosene¹¹ and nitrous oxide/propane,¹² which can be stored at atmospheric temperature, adopt the gas-liquid injection form. In demand of the development of commercial rocket engines with small thrust, the gas-liquid injection form for air oxygen/kerosene is a promising alternative method to circumvent the complexities of cryogenic fuel-providing systems.

The typical film-film pintle injector with a radial film flow colliding with an axial film flow forms a hollow conical liquid film, which undergoes the subsequent development of surface capillary waves and fragmentation to spray atomization. The spray shapes of pintle injectors with film-film injection elements^{13–15} are very similar to those of the pressure swirl injectors^{16–19} in liquid rocket engines. Vijay *et al.*²⁰ investigated the effects of internal and external flows on the primary breakup and secondary atomization of the formed liquid film of a swirl injector, for example, the core stability, breakup length, spray angle, and Sauter mean diameter (SMD). Ahn *et al.*²¹ and Khil *et al.*²² found the Klystron effects occurring in spray oscillation under the periodic change of mass flow rate, in which the spray angle varies with the disturbance of the mass flow rate, leading to non-uniformly distributed sprays and thereby the possible unstable combustions. Recently, Kang *et al.*¹⁸ investigated the effects of rocket operating environments on the spray characteristics, including the back pressure, supercritical injection, and pressure oscillation. Liu *et al.*²³ numerically investigated an annular liquid sheet sheared by a coaxial supersonic gas stream with a

swirling effect based on a large eddy simulation and found that swirling has only marginal effects on the convective instability. Kumar *et al.*²⁴ studied the mixing of constituent components transported through a narrow fluidic cylindrical channel in a swirling flow environment and found that the inlet swirl promotes advection dominated mixing, while the dominance of advection increases substantially for the higher Reynolds number. Zheng *et al.*²⁵ studied the influence of the nozzle's tangential velocity to axial velocity ratio and swirl diversion channel eccentric distance on the spray characteristics, where increase in the velocity ratio can enhance the swirl strength inside the nozzle and increase the spray cone angle. Patil and Sahu²⁶ studied the air swirl effect on spray characteristics and the droplet dispersion in a twin-jet crossflow air blast injector and found that the air swirl significantly reduces the droplet size downstream of the injector exit. A particularly useful conclusion is that increasing the swirl intensity of injection could promote the formation, breakup, and atomization of the conical liquid film, reduce the film thickness and SMD, and consequently improve the subsequent combustion characteristics.

Compared to the typical film–film injection form^{14,15} and pressure swirl injector,¹⁸ the jet–film injection^{27–29} elements uniformly distributed along the circumferential direction of the pintle are more frequently used in the practical pintle injector for the optimized spray characteristics.¹³ This is because the radial jet collides with the axial film flow with a part of the film region remaining intact with the jet flow in the circumferential direction, causing the atomized spray distributed in a wider region both in the vicinity of the axis and in the radial direction owing to the combined roles of jet and film instability mechanisms. There are many parametric studies on the spray atomization and combustion of pintle injectors, for example, the influences of geometric and flow parameters on the spray angle,^{15,27,28,30,31} the process of the film fragmentation, atomization, mixing characteristics between fuel and oxidizer,^{32–34} and spray combustion performance and stabilities.^{9,33,35}

For the gas–liquid injection form, Son *et al.*¹⁵ studied the effects of momentum ratio and flow Weber number on the spray angle of gas–film pintle injection. Yang *et al.*³⁶ experimentally and theoretically studied the spray characteristics of a recessed gas–liquid coaxial swirl injector. Wu *et al.*³⁷ experimentally studied a low-pressure intermittent air-assisted spray and focused on the effects of liquid fuel injection duration on time-resolved spray microscopic characteristics and spray unsteadiness. Khani Aminjan *et al.*^{38,39} experimentally studied the pressure swirl atomizer with tangential input and duplex air-blast atomizers spray in the engine real operation conditions. Wang *et al.*⁴⁰ studied the effects of turbulence modulation on the coaxial air-blast atomization and proposed an optimization of thread structure design for atomization improvement. Kumar and Sahu⁴¹ studied the liquid jet disintegration on spray fluctuations in a coaxial twin-fluid injector and found that the upstream unsteady jet breakup strongly influences the spatiotemporal evolution of droplet characteristics and local spray fluctuations. In addition, some papers reported experimental studies on the ignition^{42–44} and combustion characteristics⁴⁵ of the combustors with gas–liquid injection strategies.

The gas–liquid injection is superior to the liquid–liquid injection because gas injection generally has a high speed and tends to cause a strong shear on the gas–liquid interface, thereby promoting the spray atomization to smaller dispersed droplets. However, a prominent disadvantage of gas injection is that the axial gas film velocity is much

larger than that of the radial liquid jet owing to the density of the gas being much smaller than that of liquid at low throttling levels with small total chamber pressure. This leads to a very small spray angle and poor spray characteristics with spray breakup occurring only in the vicinity of the axis. To effectively solve the problem, we proposed a new design of the gas–liquid pintle injector with swirl-assisted atomization and variable swirl intensity of the swirl gas flow. The design includes two features, as the schematic shown in Fig. 1(a). First, the swirl gas flow from the tangential inlet tends to reduce the axial momentum and increase the spray angle, in which circumferential shear of the swirling gas flow promotes the atomization of the liquid jet. Second, the gas flow has two inlets where the radial and tangential inlets, respectively, provide the non-swirl and swirl gas flow, and then, the variation of swirl intensity can be achieved by assigning the total mass of gas flow into the swirl and non-swirl gas flows. In that situation, an optimized spray angle and atomization characteristics can be achieved by adjusting the swirl intensity. In addition, referring to the pressure swirl injector, the air cone formed by the swirling flow with low pressure inside might promote the jet breakup at the root position and further improve the spray characteristics.

The present work aims to experimentally verify and computationally explain our design concept of a pintle injector implemented with pressure swirl injection. The experimental apparatus and numerical methods are presented in Sec. II, followed by the experimental verification of different effects of swirl intensities on the variation of total pressure and specific impulse based on the cold flow test and the combustion test, respectively, in Sec. III, and the computational comparisons of spray characteristics, Sauter mean diameter, and droplet spatial distribution by Voronoi tessellation between three representative cases of non-swirl, half-swirl, and swirl gas flow in Sec. IV.

II. METHODOLOGY

A. Experimental apparatus

To quickly evaluate the performance of pintle injectors, it is necessary to conduct the cold flow test first because many atomization characteristics, such as the reasonable spray angle, the smaller size, and as uniform distribution as possible of the dispersed droplets, directly affect the combustion performance. The assembly and parts of the pintle injector are shown in Fig. 1(a), including three main rotating parts of a pintle, an inner sleeve, and an outer sleeve, which are nested from inside to outside with the same axis, and, respectively, provide the liquid fuel jet with an axial inlet, the non-swirl gas flow with a radial inlet, and a swirl gas flow with a tangential inlet. Different parts are flange connected.

The cold flow test rig includes two lines of high-pressure gas sources for swirl and non-swirl gas flow, one line of high-pressure gas sources to pressurize the water tank, a pressure sensor, and a high-speed camera. The pintle injector is placed in an opening space in the atmospheric environment. The water tank is pressurized to a certain pressure to ensure constant liquid injection pressure. The pressure sensor measures the injection pressure drop at the injector inlet. A high-speed camera (Phantom VEO640L) equipped with a Navitar superzoom long-distance microscopic lens is fixed and placed between the nozzle and anechoic chamber, in which the camera can ensure as many as 1400 frames per second under the S35 frame and 2560 × 1600 resolutions and the minimum exposure time of 1 μ s. The cold flow test mainly studies the effects of injection pressure drop

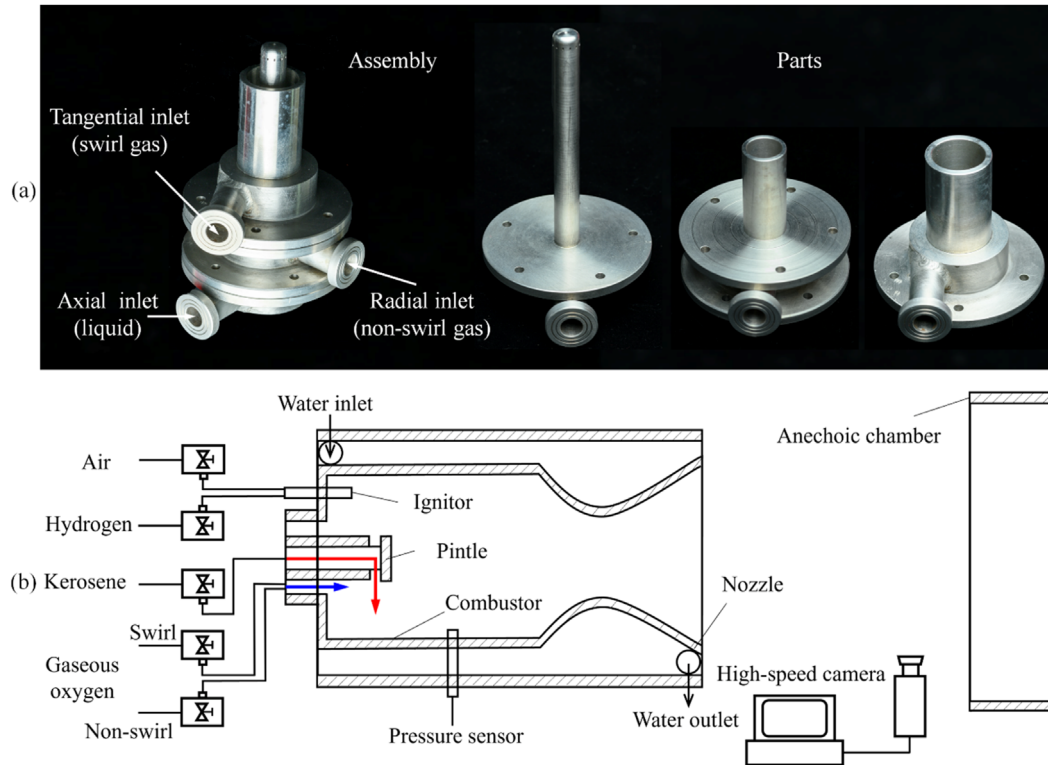


FIG. 1. (a) Assembly and parts of the swirl-assisted gas–liquid pintle injector for the cold flow test and (b) schematic of experimental apparatus for the combustion tests.

(i.e., injection velocity) and swirl effects on the spray angle and contour. The significance of the cold flow test is that the optimized spray characteristics in the cold flow test generally produce enhanced combustion performance.

The schematic of experimental settings for the combustion test of the swirl-assisted gas–liquid pintle injector is shown in Fig. 1(b). The entire testing system includes high-pressure gas sources, an ignitor, a pintle injector, a combustor, a water-cooling system, a high-speed camera, and an anechoic chamber. A line of air is connected to the kerosene tank to provide the liquid kerosene in the axial direction, and another two lines of gaseous oxygen are directly connected to the radial inlet and the tangential inlet of the pintle injector to provide non-swirl and swirl gas flow, respectively. The kerosene outlet is radial, and the gas outlet is axial, as the red and blue arrows shown in Fig. 1(b). Additional one line of air and one line of hydrogen are connected to the ignitor to ignite the kerosene sprays, in which the ignitor penetrates through the injector panel into the combustor and offset to the side of the pintle injector head. The combustor is nested into the water-cooling system with a water inlet on the left and a water outlet on the right. After the nozzle, it is implemented an anechoic chamber to reduce the noise and capture the unburn kerosene after the nitrogen gas washing.

The present combustion test measures two main parameters of the total pressure and thrust. The total pressure is measured by a pressure sensor that is connected to a through hole of the combustor, and the thrust is measured by a dynamometer directly connected to the combustor base. The pressure sensor (GE, UNIK 5000) measures the total pressure in the range of 0–20 MPa with the sampling frequency

of 3.5 kHz and the uncertainty of $\pm 0.1\%$. The thrust is measured by a sensor (OMEGA, LC203-500) with the uncertainty of $\pm 0.05\%$. In addition, there are many other pressure sensors connected to every valve and gas line to monitor the injection pressure, thereby the mass flow rate of gaseous oxygen and liquid kerosene. The mass flow rate of kerosene is controlled by a proportioning valve (Bosch Rexroth, R901239141) and can be directly measured by a turbine flowmeter (OMEGA, FTB-1312). The measured errors are generally $\pm 1.0\%$ with the variation of mass flow rate in the range of 23–2330 g/s. The gas mass flow rate is controlled by changing the upstream pressure through a high-precision pressure regulator (Emerson, ER5000 Electropneumatic Actuator). Again, a high-speed camera (Phantom VEO640L) equipped with a Navitar superzoom long-distance microscopic lens is fixed and placed between the nozzle and anechoic chamber, in which the camera can ensure as many as 1400 frames per second under the S35 frame and 2560×1600 resolutions and the minimum exposure time of $1 \mu\text{s}$. The spatial resolution of the camera in terms of pixel to millimeter is about 0.01 mm for each pixel. It also uses another normal colorful digital camera to capture the fire shape and relevant shock trains. The entire running time of the experiment is about 16 s, in which the combustion process lasts for 6–8 s so that stable combustion can be established and thereby accurate measurement of thrust and total pressure.

B. Numerical method and specifications

The three-dimensional (3D) continuity and incompressible Navier–Stokes equations,

$$\nabla \cdot \mathbf{u} = 0, \quad (1)$$

$$\rho(\partial \mathbf{u} / \partial t + \mathbf{u} \cdot \nabla \mathbf{u}) = -\nabla p + \nabla \cdot (2\mu \mathbf{D}) + \sigma \kappa \mathbf{n} \delta_s, \quad (2)$$

are solved by using the classic fractional-step projection method, where \mathbf{u} is the velocity vector, ρ the density, p the pressure, μ the dynamic viscosity, and \mathbf{D} the strain rate tensor defined as $D_{ij} = (\partial_j u_i + \partial_i u_j) / 2$. In the surface tension term $\sigma \kappa \mathbf{n} \delta_s$, δ_s is a Dirac delta function, σ the surface tension coefficient, κ the local curvature, and the unit vector \mathbf{n} normal to the local interface. The present study adopts the volume-of-fluid (VOF) method. To solve both the gas and liquid phases, the density and viscosity are constructed by the volume fraction as $\rho = c\rho_l + (1-c)\rho_g$ and $\mu = c\mu_l + (1-c)\mu_g$, in which the subscripts l and g denote the liquid and gas phases, respectively. The volume fraction c satisfies the following advection equation:

$$\partial c / \partial t + \nabla \cdot (c\mathbf{u}) = 0 \quad (3)$$

with $c = 1$ for the liquid phase, $c = 0$ for the gas phase, and $0 < c < 1$ for the gas-liquid interface.

In the present study, the pure Eulerian approach with the VOF method implemented in the open source code, Gerris,^{46–48} is adopted to analyze the spray characteristics. Gerris features the 3D octree adaptive mesh refinement, the geometrical VOF interface reconstruction, and continuum surface force with height function curvature estimation, which has been demonstrated to be competent for high-fidelity simulation of the breakup of liquid jets^{49,50} and films and subsequent spray atomization.^{51–54} The full VOF simulation of sprays is a direct numerical simulation (DNS)^{55,56} and can accurately predict the primary breakup of liquid jet or film and provide as many details of sprays as possible if using appropriate mesh resolution to certain physical problems. However, a major challenge of DNS lies in the extremely fine mesh resolution for large numbers of dispersed droplets and secondary breakup and thereby substantial computational cost. For example, Salvador *et al.*⁵³ analyzed the effects of turbulent inflow conditions on the primary breakup of a liquid jet by DNS with approximately 66×10^6 cells and a minimum cell of $2.34 \mu\text{m}$. Shinjo and Umemura⁵⁶ performed a DNS of the primary breakup of a liquid jet with a total mesh number of nearly 6×10^9 to resolve the minimum mesh grid of $0.35 \mu\text{m}$. To improve the computational efficiency, the coupled Eulerian-Lagrangian approach^{52,57–60} was proposed to combine the Eulerian method for the primary breakup of liquid jet or sheet and the Lagrangian model for the dispersed droplet dynamics, where all droplets with diameters smaller than the reference value would be transformed into Lagrangian particles.

It is worth mentioning that the present simulation is, however, not focused on resolving spray details as much as possible but on the computational explanations of our design concept of a pintle injector implemented with pressure swirl injection. Thus, the total mesh number in the present simulation based on the adaptive mesh is about 8×10^6 (minimum mesh grid of $30 \mu\text{m}$), which is prominently less than that of 6×10^9 (minimum mesh grid of $0.35 \mu\text{m}$) for the simulation of a jet breakup⁵⁶ based on a uniform mesh.

The present VOF simulation is limited to the cold flow spray of kerosene without ignition and combustion because a good spray characteristic with an optimized spray angle and small discrete droplets distributed as uniformly as possible tends to lead to a good combustion performance. The comparisons of spray angle and spray characteristics between the simulation and experiments have been discussed

sufficiently in our previous work.⁶¹ The comparison of the probability density function (PDF) of dispersed droplet diameter for different mesh resolutions demonstrates the inherent drawbacks of a full VOF simulation in dealing with the primary breakup of jet or film: strong grid dependence of PDF and substantial computational costs for the secondary breakup of sprays. To balance the accuracy and computational cost, the present study chooses the same mesh refinement level⁶¹ of ($N_0 = 3$ and $N_d = 5$) and mainly focuses on comparing the swirl flow effects on spray characteristics in the same frameworks, in which N_0 and N_d are the initial and maximum mesh refinement levels for the gas and the gas-liquid interface zones, respectively. Generally, N_d for the gas-liquid interface zone plays a dominant role in jet or film breakup characteristics, and N_0 for the gas zone reduces the total number of meshes.

Figure 2 shows the schematic of the computational domain and geometrical parameters of a swirl gas-liquid pintle injector. The liquid inlet is axial with a characteristic diameter D , and the liquid outlet radially consists of 12 injection orifices, in which the shape of each orifice is a square connected by two semicircles on two sides. Both the length of the square and the diameter of the semicircle are $0.075D$. The gas has two inlets with the same diameter of $0.75D$, namely, radial inlet and tangential inlet, respectively, providing non-swirl gas flow and swirl gas flow. The non-swirl and swirl gas flows are compounded into one swirl flow and then injected from the axial annular exit with a thickness of $0.15D$. The 3D computational domain is $42D$ in length along the axial direction and $40D$ in width and height perpendicular to the axial direction. All boundaries except inlets are specified as free outflow boundary conditions.

For the representative case, it simulates multiple kerosene jets in the radial direction colliding with an annular film of gaseous oxygen in the axial direction at the pressure environment of 2 MPa, in which the density, viscosity, and surface tension coefficient for liquid kerosene are $\rho_l = 0.76 \times 10^3 \text{ kg/m}^3$, $\mu_l = 2.30 \times 10^{-3} \text{ N s/m}^2$, and $\sigma = 2.65 \times 10^{-2} \text{ N/m}$, respectively; the density and viscosity for gaseous oxygen at 2 MPa are $\rho_g = 28.6 \text{ kg/m}^3$ and $\mu_g = 2.03 \times 10^{-5} \text{ N s/m}^2$, respectively. The injection velocities of liquid kerosene and gaseous oxygen are $v_l = 17.22 \text{ m/s}$ and $v_g = 150.43 \text{ m/s}$, respectively. Consequently, the liquid Weber number and the Ohnesorge number for the liquid jet can be calculated as $We = 8500$ and $Oh = 1.62 \times 10^{-2}$, in which the collision Weber number, $We = \rho_l D v_l^2 / \sigma$, measures the relative importance of the jet or film impact energy compared to the surface energy, and the Ohnesorge number, $Oh = \mu_l / \sqrt{\rho_l D \sigma}$, measures the relative importance of the liquid viscous stress compared to the capillary pressure. The dimensionless time is defined as $T = \frac{t}{t_{\text{ine}}}$, and the characteristic collision time is $t_{\text{ine}} = D / v_l = 0.058 \text{ ms}$. A typical simulation run results in about 8.0×10^6 grid points in the entire domain by fixing $N_0 = 3$ and $N_d = 5$ for all cases and takes about 200 h of real time to simulate up to $T = 0.2$ on an AMD EPYC 7452 processor with 64 cores.

III. EXPERIMENTAL RESULTS

A. Swirl effects on spray angle

Figure 3 compares the experimental images of sprays with pure radial jet, non-swirl gas flow, and swirl gas flow in the atmospheric environment. The injection pressure drop of liquid water is 0.25 MPa, approximately corresponding to the injection velocity of 20 m/s and

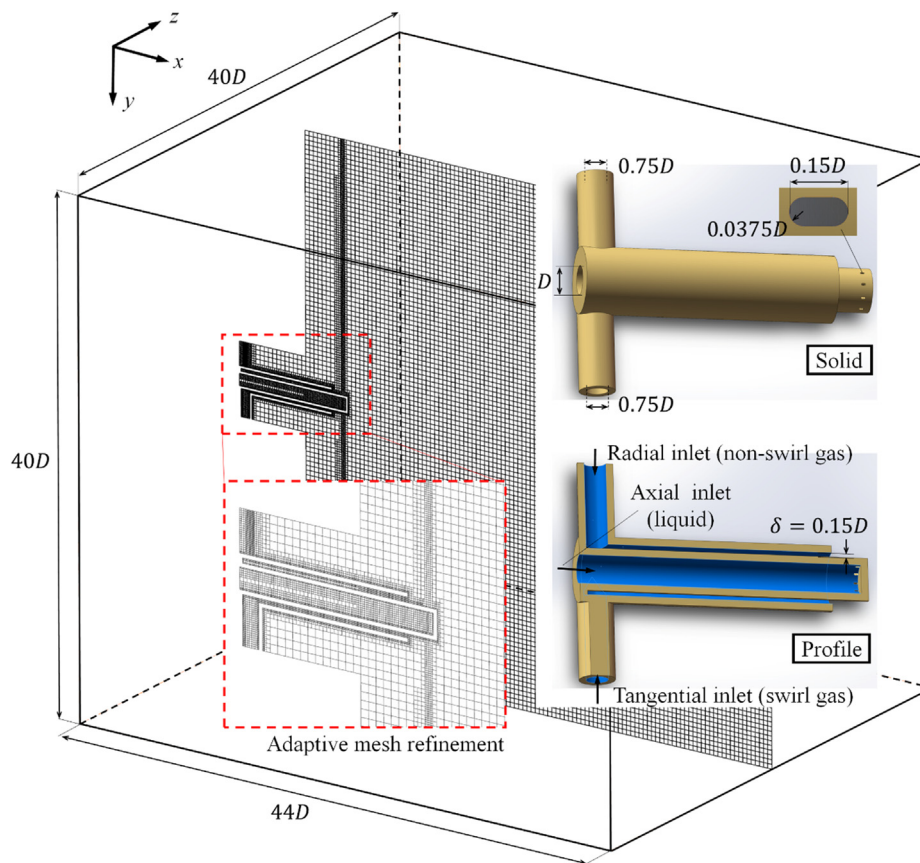


FIG. 2. Schematic of the computational domain and geometric parameters of a swirl gas-liquid pintle injector with an axial liquid inlet, a radial gas inlet, and a tangential gas inlet.

the mass flow rate of $\dot{m} = 90 \text{ g/s}$. As the spray contour and closeup shown in Fig. 3(a), 12 jets are observed from the injection orifices distributed uniformly along the circumferential direction of the pintle. The primary breakup of the jets into liquid filaments occurs due to the hydrodynamic instability, and discrete droplets in downstream beyond the present frame are not shown in the figure.

Upon the injection of liquid into gas, the liquid jet is rapidly atomized into substantially dispersed droplets, in which the mass flow rate of gas is about $\dot{m} = 154 \text{ g/s}$ and the injection velocity of the gas is nearly the speed of sound in the standard atmospheric environment. Apart from the representative instants of the spray contour for the non-swirl and swirl gas flows shown in Figs. 3(b) and 3(c), the time evolution of the spray angle to characterize the temporal fluctuations is also shown in Fig. 3(d). The spray angle θ is quantitatively defined as $\tan \theta = H/L$, where H and L are, respectively, the radial and axial distances from the boundary point at the camera frame to the liquid injection inlet, with the boundary point separating the liquid spray on the left and the environment gas on the right, as shown in Figs. 3(b) and 3(c). The frame used in the current experiment is S35 ($25.6 \times 16 \text{ mm}$) with 2560×1600 resolutions and $10 \mu\text{m}$ for each pixel. For the cold flow test, the images are exposed with a $9\text{-}\mu\text{s}$ shutter and the spray angle is measured within a 10% error. It is seen two approximate plateaus with about 30° and 45° for the non-swirl and swirl gas flow, respectively, and the transition connects the two stable operating conditions, which indicates that the swirl gas flow increases the spray angle

and leads to a broader distribution of dispersed droplet. The good spray characteristics tend to simultaneously have a small Sauter mean diameter and a broad distribution of dispersed droplets in the combustor. Although the diameters of the dispersed droplets were not measured in the test, a more uniform distribution of dispersed droplets by the swirl gas flow injection is inferred to improve the spray characteristics. In addition, the spray angle and the spatial distribution of dispersed droplets can be adjusted by varying the mass flow rate of non-swirl and swirl gas flow, which enhances the flexibility of performance control and simplifies the match between injection pressure drop and injection area for the variable mass flow rate condition.

B. Swirl effects on total pressure and specific impulse

This section focuses on the swirl effects of gas flow on the spray characteristics and combustion performance, in which the deviation of total pressure and specific impulse between the experimental measurement and the theoretical estimation serves as an indicator for effective spray and combustion. For the convenience of description, the swirl flow ratio (SFR) is defined to characterize different swirl intensities of the compounded swirl gas flow and controlled by reassigning the total gas flow from the either radial inlet or tangential inlet, with $\text{SFR} = 1.0$ the pure swirl flow and $\text{SFR} = 0.0$ the pure non-swirl flow. Similarly, the mixture ratio (MR) characterizes different mass ratios of gaseous oxygen to liquid kerosene. The detailed experimental parameters for

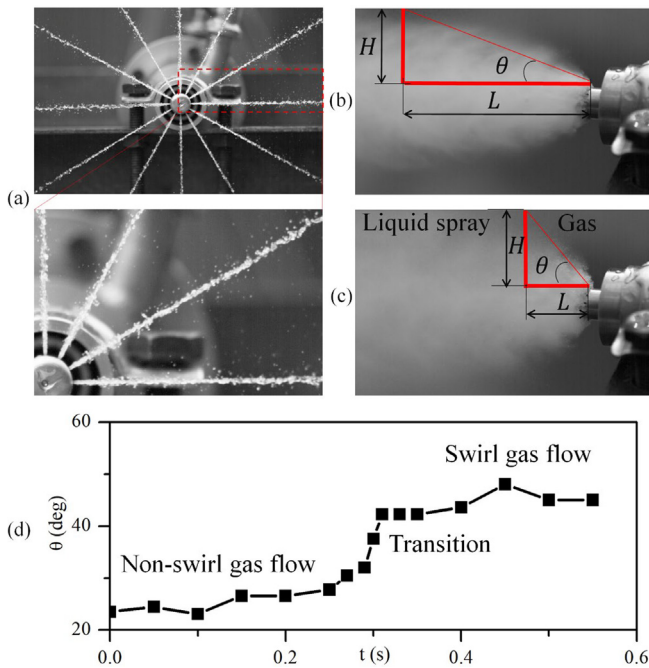


FIG. 3. Experimental images of the cold flow test in the atmospheric environment for the pintle injector with (a) radial liquid jet only, (b) non-swirl gas flow, (c) swirl gas flow, and (d) evolution of the spray angle θ to show the temporal fluctuations of the spray.

all 11 cases, including the mass flow rates and outlet velocities for the non-swirl, swirl gas flow, and kerosene, are presented in Table I.

Figure 4 shows the experimental images of the flame for different cases shown in Table I. A chain of shock waves out of the nozzle with $MR = 3.5$ is shown in Fig. 4(a), and the numbers of shock waves are 7,

TABLE I. Experimental parameters for different swirl intensities and mixture ratios.

Cases	Non-swirl oxygen \dot{m}_{ns} (g/s)	Swirl oxygen \dot{m}_s (g/s)	Kerosene \dot{m}_l (g/s)	Oxygen outlet velocity (m/s)	Kerosene outlet velocity (m/s)	MR ^a	SFR ^b
1	201.3	0.0	108.2	179.9	17.5	1.86	0.0
2	50.3	150.5	108.4	161.1	17.7	1.85	0.25
3	100.6	98.1	108.0	168.4	17.5	1.84	0.50
4	154.0	50.6	109.0	179.1	17.6	1.88	0.75
5	0.0	201.4	106.6	199.0	17.3	1.89	1.0
6	171.9	0.0	131.0	165.7	21.2	1.31	0.0
7	85.8	86.2	131.8	161.8	26.9	1.31	0.5
8	0.0	171.8	131.0	191.9	21.3	1.31	1.0
9	97.7	0.0	27.7	237.9	4.49	3.53	0.0
10	49.5	50.4	27.7	235.1	4.48	3.61	0.5
11	0.0	101.0	27.5	266.5	4.45	3.67	1.0

^aMixture ratio (MR): mass ratio of gaseous oxygen ($\dot{m}_{ns} + \dot{m}_s$) to liquid kerosene \dot{m}_l .
^bSwirl flow ratio (SFR): mass ratio of swirl gas flow \dot{m}_s to the total gas flow ($\dot{m}_{ns} + \dot{m}_s$).

6, and 5 for the non-swirl ($SFR = 0.0$), half-swirl ($SFR = 0.5$), and swirl ($SFR = 1.0$) gas flows, respectively. This is because that MR is larger than the stoichiometric oxidizer/fuel ratio, so the kerosene tends to be sufficiently burned out showing the blue flame color. As decreasing MR with the insufficient combustion of kerosene, the flame color turns yellow and then, the shock wave chain is difficult to be observed with the setting of the light source and exposure based on the colorful camera. Figure 4(b) shows the time sequence images for case 5 using the high-speed camera. For the combustion test, the nozzle outlet and flame width are in the order of $O(10^{-1})$ m. Apart from the beginning and ending time instants, the flame shape is approximately stable with only slight fluctuations. To quantitatively characterize the flame fluctuations and combustion stability, the evolution of the instantaneous flame width and chamber pressure is measured and shown in Fig. 5, in which the flame width l is normalized with a characteristic length L . The results show that the width ratio l/L fluctuates between about 0.75–1.25 and the average value is about the unity during an oscillating period. In addition, the measured chamber pressure for representative cases with different SFR is approximately constant during the combustion time from 10 to 16 s, which confirms that the combustion system is stable and the measured total pressure and specific impulse are accurate.

Figure 6 quantitatively compares the total pressure P_t and the specific impulse I_s between the theoretical estimations and experimental measurements for all cases shown in Table I. All combustion test is performed at least one more time so as to obtain the stable total pressure curve and thrust curve. The theoretical P_t and I_s are estimated by a NASA Open-Source Program, CEA,^{62–64} in which the input parameters include the chamber pressure, the mixture ratio, the mass flow rate per unit chamber section area, and the nozzle expansion ratio. For those cases 1–8 at 2 MPa, the nozzle expansion ratio equals 3.16 with the nozzle under-expansion. For cases 9–11 at 1 MPa, the nozzle expansion ratio is the chamber pressure to the standard pressure because the nozzle is excessive expansion. The results show that the theoretical total pressure and specific impulse vary slightly with SFR because the total mass flow rate and MR are constant, and the experimental measurements of P_t and I_s have an approximately 10%–20% loss compared with the theoretical values.

A prominent finding is that the experimental P_t and I_s are largest at $SFR = 1.0$, which indicates that the swirl gas flow can improve the spray characteristics and subsequent combustion performance to ensure sufficient spray combustion that is as much close to the ideal situation as possible. However, it shows a non-monotonic variation of P_t and I_s with varying SFR and have a minimum value at $SFR = 0.5$ with the half-swirl gas flow. This indicates that the swirl effects of gas flow are possibly not always beneficial to the enhancement of combustion efficiency, which may depend on the local spray characteristics owing to the interaction between non-swirl and swirl gas flow inner the injection tube and merit further computational study in the following. In addition, a larger MR for cases 1–5 favors the larger P_t and I_s owing to the enhanced combustion efficiency with MR closer to the stoichiometric ratio.

IV. COMPUTATIONAL VERIFICATIONS OF SWIRL-ASSISTED SPRAY

A. Spray contour

Figure 7 compares the spray contour affected by different swirl gas flow intensities. The gas and liquid phases are denoted by transparent

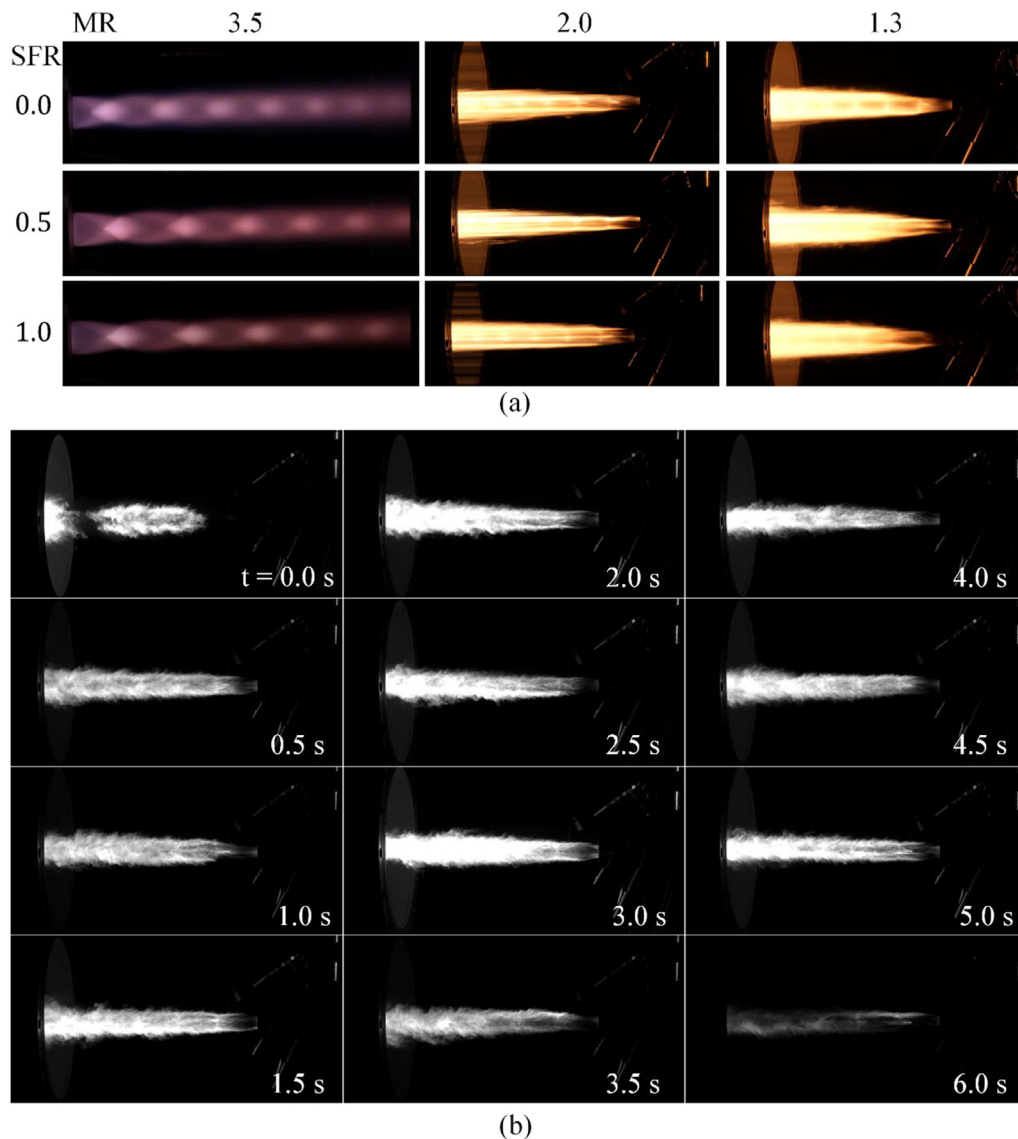


FIG. 4. Experimental images of the combustion test for (a) different cases with varying mixture ratios (MR) and swirl flow ratios (SFR) and (b) time sequence images by using the high-speed camera for the representative case 5.

blue and dark red, respectively. The results are illustrated from two different views at the x - y plane and y - z plane on the first and second rows, respectively, to show the 3D characteristics of sprays, in which the white dash line is the rotating axis of the pintle injector. To clearly illustrate the spatial characteristics of sprays, the co-ordinate is shown for each case and all co-ordinate values at x -, y -, and z - directions have been scaled with a factor of 0.1.

For the pure non-swirl gas flow (SFR = 0.0) shown in Fig. 7(a), the spray contour is approximately axisymmetric based on the x - y or x - z plane in the early stage of sprays and shows slightly non-axisymmetric in the late stage of sprays, which is probably caused by the radial inlet of gas flow that offset to only one side of the pintle injector. The penetration distance reaches about 5.0 at

$T = 0.172$ for the non-swirl gas flow shown in Fig. 7(a). For the pure swirl gas flow (SFR = 1.0) shown in Fig. 7(c), the penetration distance is substantially reduced to about 3.0 at $T = 0.172$ because the swirl effects reduce the axial momentum and partially convert the original axial momentum into the circumferential counterpart. It is seen a prominent asymmetry of the spray contour in the late stage of sprays. To compensate for the reduced penetration distance and enhanced asymmetry of the spray contour, the half-swirl gas flow (SFR = 0.5) is simulated and shown in Fig. 7(b). The penetration distance reaches about 4.0 at $T = 0.172$ and is intermediate between the pure non-swirl and pure swirl gas flow cases. In addition, the spray contour is approximately axisymmetric during the entire spray process.

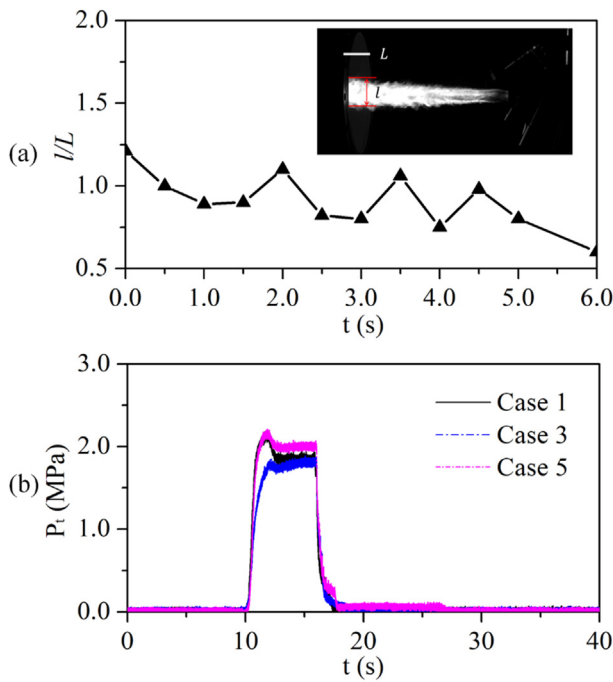


FIG. 5. Time evolution of the (a) flame width ratio and (b) measured chamber pressure for different cases.

It is noted that the asymmetric spray contour is probably only for the pintle design in the present study, which is attributed to the non-uniform velocity distribution caused by a radial inlet and a tangential inlet that offset two sides of the pintle injector. The asymmetry of gas flow influencing the spray characteristics merits further study and is beyond the scope of the present study. In addition, it is hard to evaluate spray characteristics only according to the spray contour, and the quantitative analysis of Sauter mean diameter and Voronoi tessellation is necessitated and discussed in the following.

B. Sauter mean diameter

Figure 8 shows the probability density function (PDF) of droplet diameters and characteristic volume-to-surface length for three different swirl flow ratios. It is seen that all the curves of PDF and volume-to-surface length are approximately overlapped for these three cases, in which the PDF shows a Poisson distribution with a diameter of about $90 \mu\text{m}$ at the peak of PDF, and the characteristic volume-to-surface length is about $O(100) \mu\text{m}$ and decreases as the evolution of sufficient breakup of liquid jet or film, as shown in Fig. 7. It is noted that the PDF and volume-to-surface length characterize the global properties of the spray, and some quantities to characterize the local properties of the spray are necessitated.

The statistical distribution of atomized droplet size can be quantified by the characteristic diameter.⁶⁵ The discrete form of characteristic diameter is defined as follows:

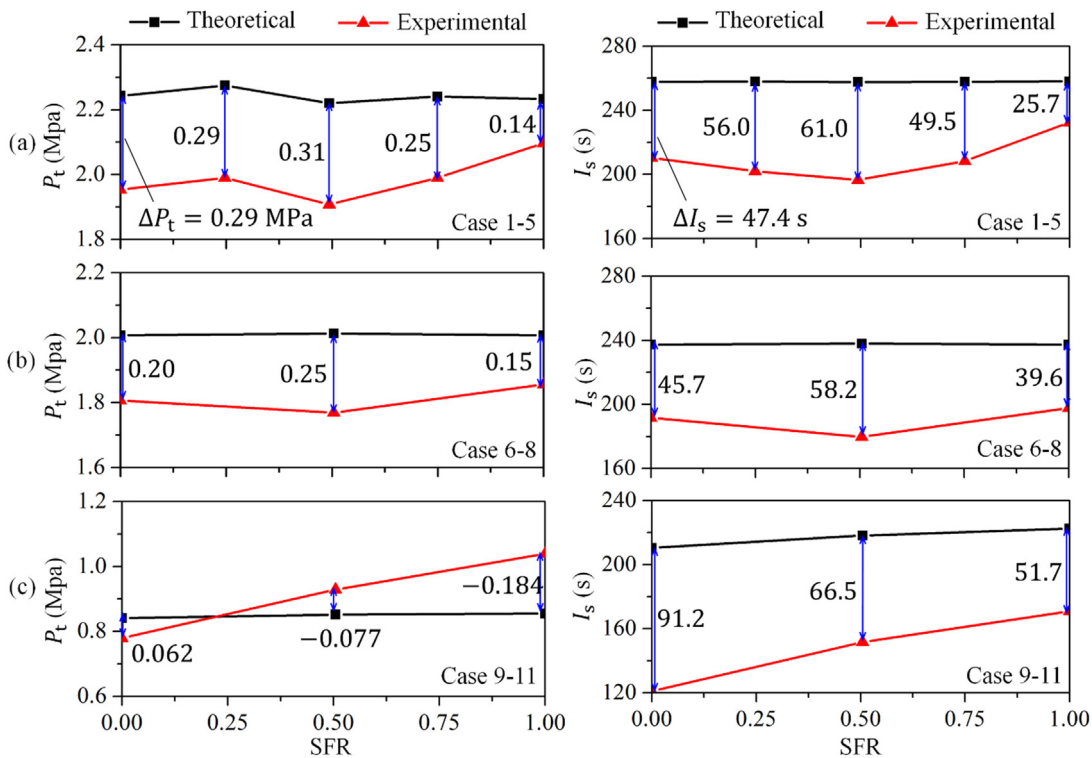


FIG. 6. Comparison of the total pressure P_t and the specific impulse I_s between the theoretical estimation and the experimental measurement for (a) cases 1–5, (b) cases 6–8, and (c) cases 9–11.

08 April 2024 03:00:56

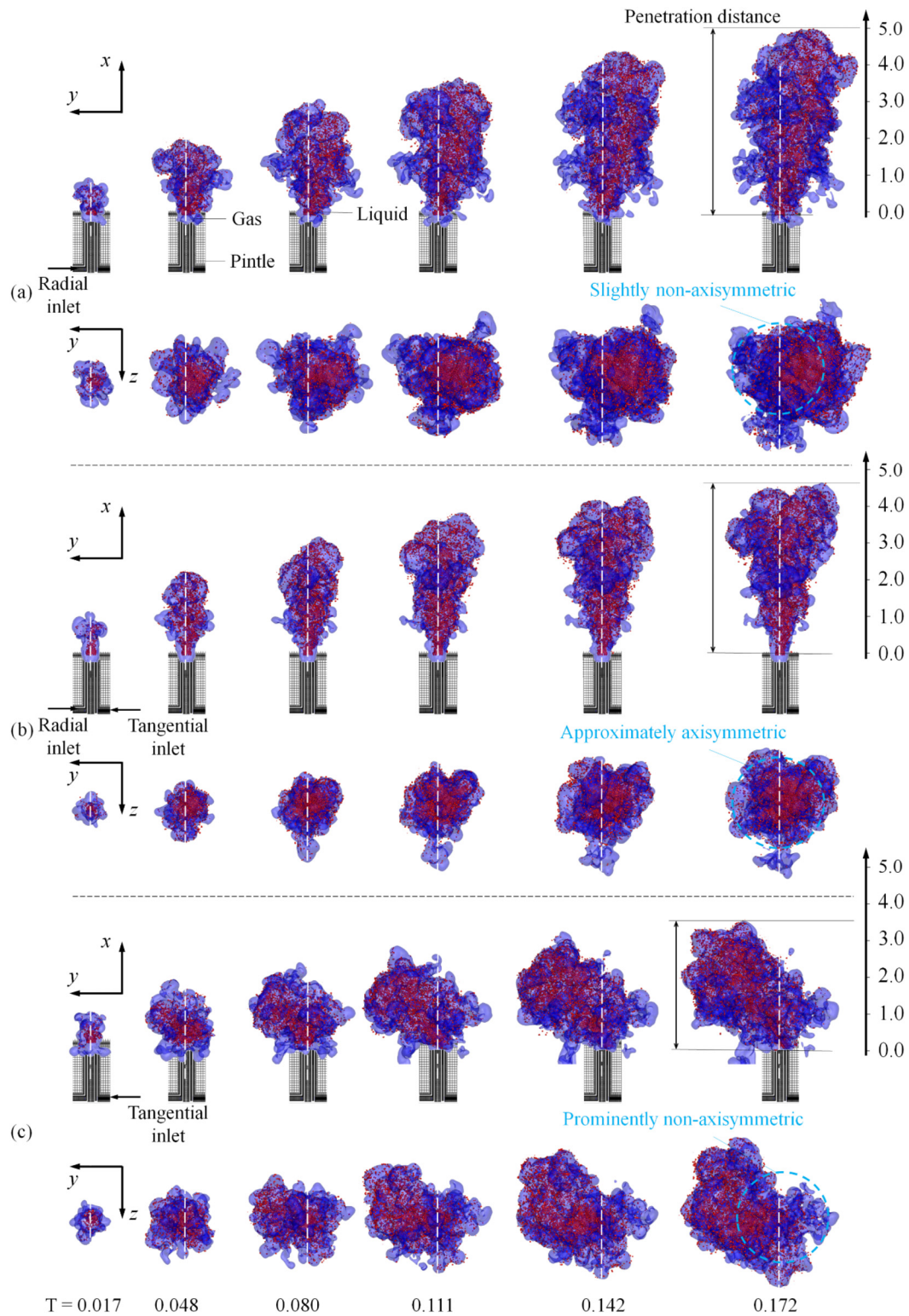


FIG. 7. Comparison of spray contours (red for liquid and blue for gas) between three representative cases with different swirl flow ratios (SFR). (a) SFR = 0.0, (b) SFR = 0.5, and (c) SFR = 1.0.

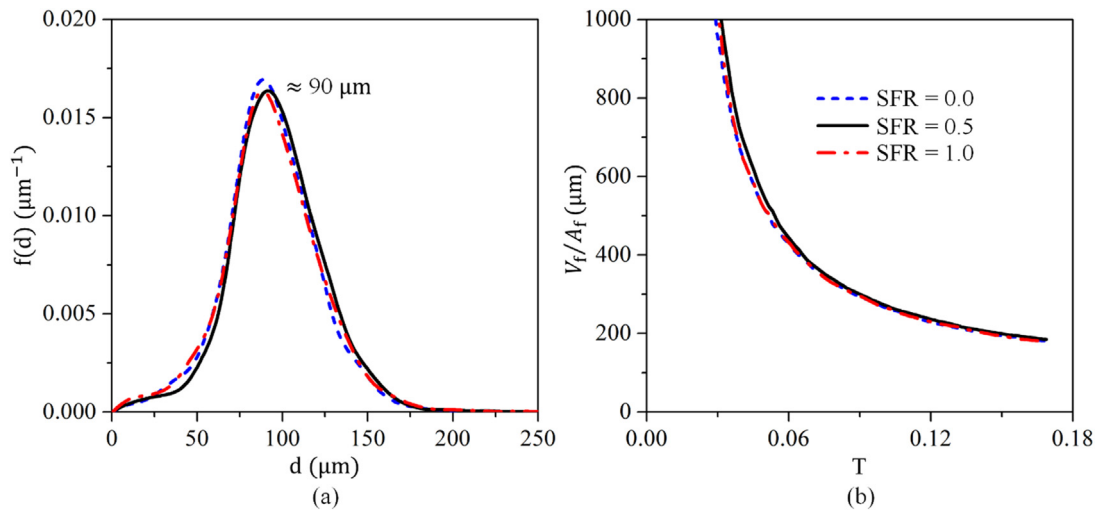


FIG. 8. Comparison of (a) probability density function (PDF) of discrete droplets diameter and (b) characteristic volume-to-surface length for three cases shown in Fig. 7 with different swirl flow ratios (SFR).

$$D_{pq} = \frac{1}{t} \sum_{\Delta t=1}^t \left[\frac{\sum_{i=1}^{\infty} n_i D_i^p}{\sum_{j=1}^{\infty} n_j D_j^q} \right]^{1/(p-q)}, \quad (4)$$

where p and q are positive integers, n the number of droplets with a diameter of D , and t the number of total discrete sampling time. In general, the Sauter mean diameter (SMD), D_{32} , is the most representative one that measures the volume-to-surface ratio of a finite fluid parcel. Figure 9 compares the time-averaged SMD contour at different x co-ordinates in the axial direction during a small time period before and after the representative instant at $T = 0.172$, in which the small time period is about $\Delta T = 0.02$ containing about ten numerical steps. For all three cases, the contour results show that there are not any prominent regions with the SMDs being larger than $200 \mu\text{m}$, and the majority of the SMD is distributed around $100 \mu\text{m}$ owing to sufficient atomization. However, it is seen the differences in the spatial distribution of SMD for three cases. Specifically, for the half-swirl gas flow (SFR = 0.5) shown in Fig. 9(b), the region of nonzero SMD at $x = 0.5$ is smallest and the SMD at its central position is larger than $200 \mu\text{m}$, which leads to the insufficient spray atomization in the vicinity of the pintle head. For the pure swirl gas flow (SFR = 1.0) shown in Fig. 9(c), although the spray penetration distance in the x -direction is shortest owing to the reduced axial momentum by the swirl gas effects, the region of nonzero SMD is much broader than other two cases both at $x = 0.5$ that close to the pintle head and also on other slices. It indicates that the swirl gas effects can promote the earlier breakup of liquid jet or film and thereby enhance the spray characteristics. The SMD contour at $x = 3.5$ for the swirl gas flow is negligible and thereby not presented in Fig. 9(c).

The swirl gas effects break the axisymmetric flow of the traditional jet-film pintle injector and lead to rich local characteristics of sprays that merit further analysis. The spray contour for SFR = 1.0 shows prominent asymmetry at one certain time and may appear an

axisymmetric and time-averaged spray contour for a long period of time. However, apart from the time-averaged characteristics, the instantaneous characteristics are also significant to the spray and combustion characteristics. Although the contour of the SMD value shows slight differences, the SMD distribution varies greatly by the swirl gas effects. The sufficient spray atomization tends to simultaneously have a smaller SMD and also a uniform distribution of dispersed droplets, which motivates us to analyze the atomized droplets by using the Voronoi tessellation in the following.

C. Voronoi tessellation

As discussed above that a very common approach to evaluating the spray characteristics is using the SMD,^{29,65,66} however, a spray with locally small SMD does not guarantee good combustion performance because SMD does not reflect the droplet clustering characterizing the interaction between neighboring droplets. To analyze the spatial distribution of dispersed droplets, Srikrishna^{67–69} proposed an approach to analyzing droplet clustering from the topological aspects by using the Voronoi tessellation. As the 2D example shown in Fig. 10, Voronoi tessellation^{67,68,70,71} divides the entire space into many subspaces around droplets so that every point in a subspace is closer to its corresponding droplet co-ordinate than other droplets. As a result, the points on a boundary between two subspaces have the same distance to the droplets belonging to the subspaces. Voronoi tessellation can be mathematically described as that, for each droplet j occupying the co-ordinate \mathbf{x}_j , its influence region $R(j)$ is defined as follows:

$$R(j) = \left\{ \mathbf{x} \in \mathbb{R}^n \mid d^0(\mathbf{x}, \mathbf{x}_j) \leq d^0(\mathbf{x}, \mathbf{x}_k), \quad \text{for all } k \neq j \right\}, \quad (5)$$

where \mathbf{x} is the coordinate for a droplet in the Euclidean space \mathbb{R}^n (n is the dimension, $n = 2$ or 3 in the present study), and

$$d^0(\mathbf{x}, \mathbf{x}_k) = |\mathbf{x} - \mathbf{x}_k| = \left[\sum_{i=1}^n (x^i - x_k^i)^2 \right]^{1/2} \quad (6)$$

is the natural Euclidean metric (distance function).

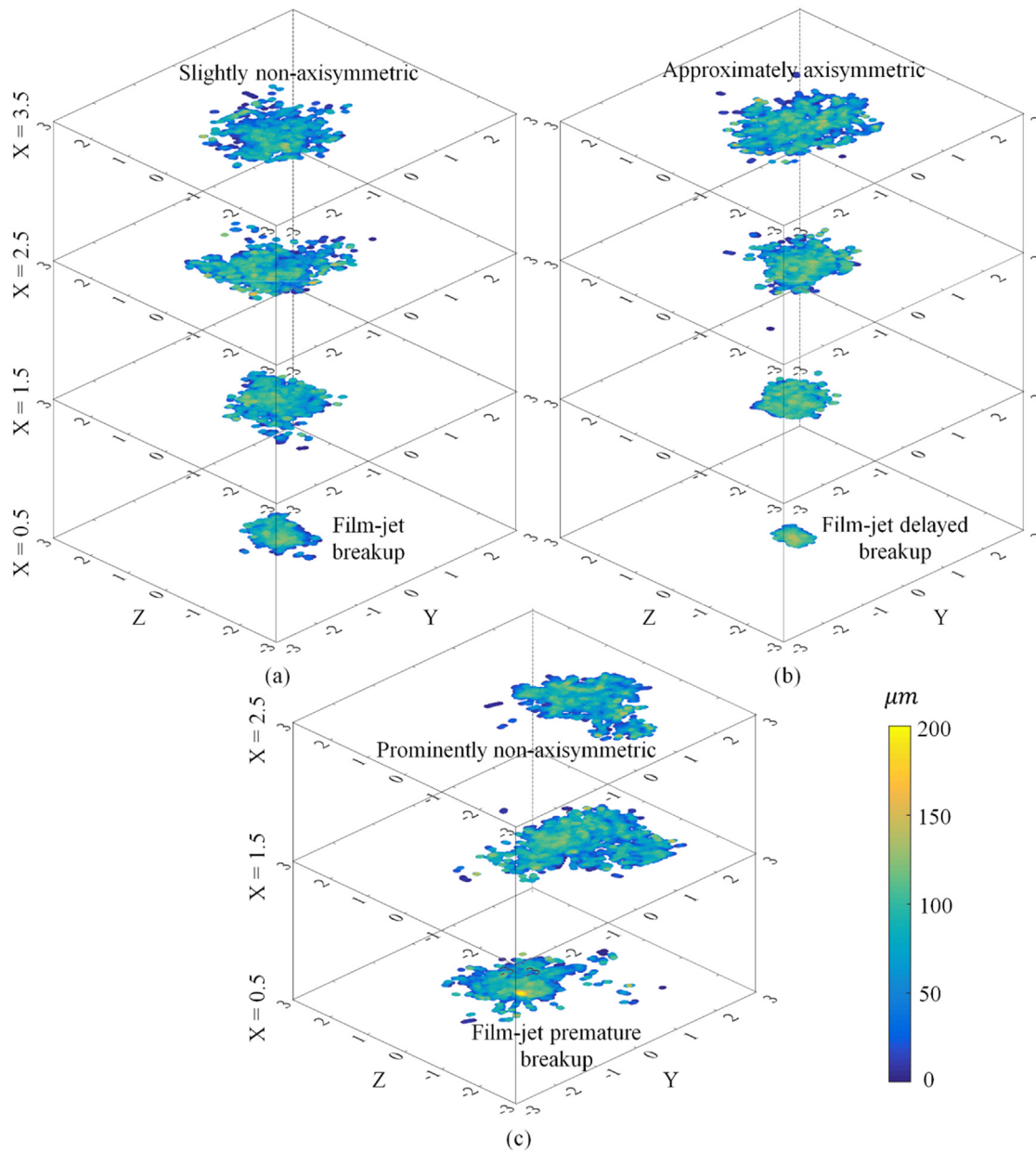


FIG. 9. Comparison of 2D distribution of Sauter mean diameter (SMD) on different slices along the axial (x -) direction for three cases shown in Fig. 7. (a) SFR = 0.0, (b) SFR = 0.5, and (c) SFR = 1.0.

Figure 10 shows the Voronoi diagram at different x coordinates for the three representative cases. It is seen in the dense spray with a large number density of dispersed droplets or small Voronoi volumes close to the pintle head, as $x = 0.5$ and 1.5 shown in Fig. 10(b), and the dilute spray with the small number density of dispersed droplets or large Voronoi volumes far away from the injector, as $x = 1.5$ and 2.5 shown in Fig. 10(c). Overall, the spatial distribution range of Voronoi cells is approximately consistent with the region of nonzero SMD contour shown in Fig. 9. However, the results show that there is

no prominent correlation between SMD and Voronoi volumes. For example, the white squares 1 and 2 at $x = 1.5$ shown in Fig. 11(a) have a similar SMD distribution but correspond to a dense spray (small Voronoi volumes) in square 1 and a dilute spray (large Voronoi volumes) in square 2. Similarly, for the swirl gas flow case at $x = 2.5$ shown in Fig. 11(b), the volumes of Voronoi cells vary prominently for approximately the same SMD value. It indicates that both the Voronoi diagram and the SMD contour are significant to evaluate the spray characteristics because they reflect two different aspects

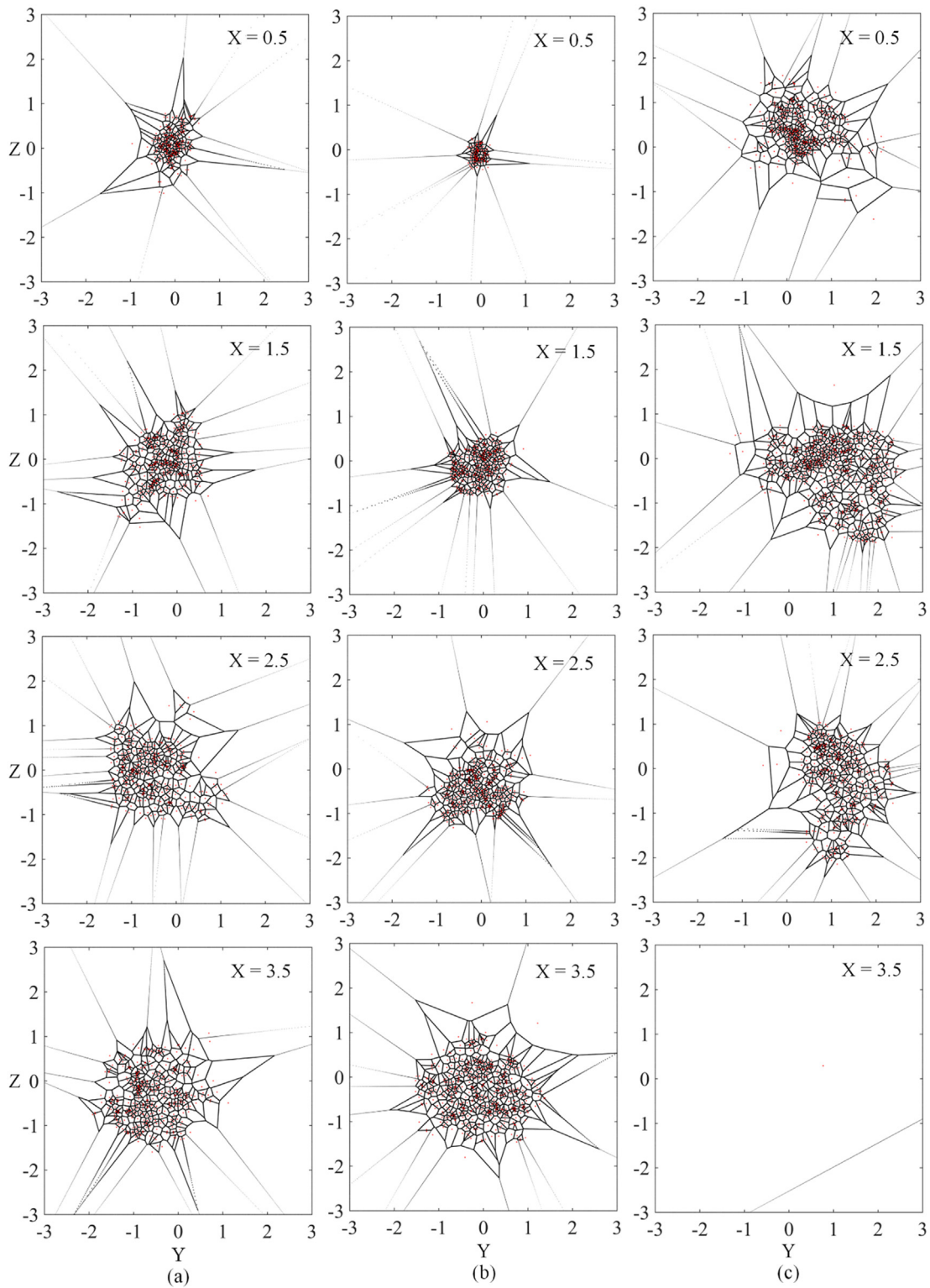


FIG. 10. Comparison of Voronoi diagram of all discrete droplets on the slices along the axial (x -) direction for three cases shown in Fig. 7. (a) $SFR = 0.0$, (b) $SFR = 0.5$, and (c) $SFR = 1.0$.

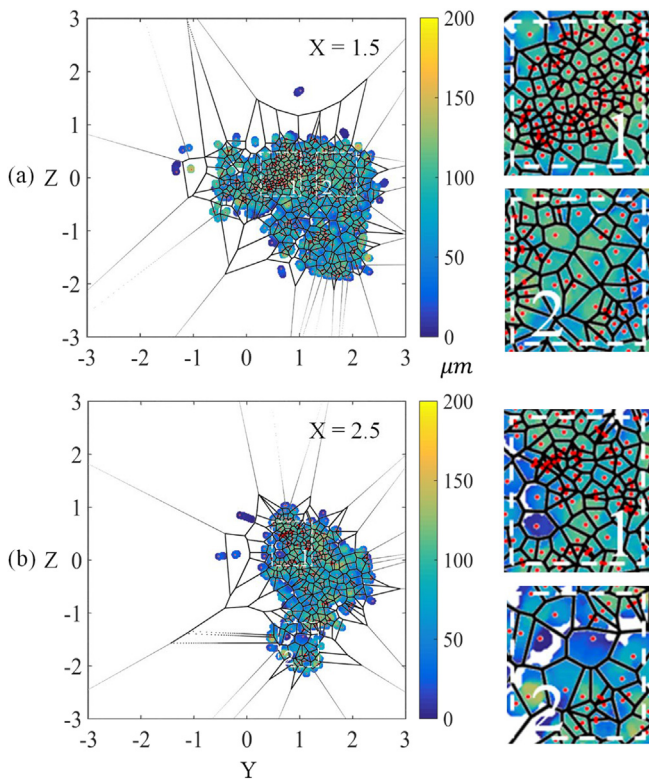


FIG. 11. Spatial distribution of SMD contour and Voronoi diagram at (a) $X = 1.5$ and (b) $X = 2.5$, respectively.

of the spray. The SMD contour reflects the time average of discrete droplets at a certain spatial location, whereas the Voronoi cells reflect the local characteristics of discrete droplet distribution at a certain time.

Figure 12 further compares the number, the mean Voronoi volume, and the square standard deviation of Voronoi volumes at different slices for the three representative cases. The variation trends of the number and mean Voronoi volume for the non-swirl gas flow (SFR = 0.0) and the half-swirl gas flow (SFR = 0.5) are approximately the same except some prominent differences of the spray at $x = 0.5$, in which a smaller number of dispersed droplets and a larger mean Voronoi volume for SFR = 0.5 are attributed to the delayed breakup of liquid jet or film in the vicinity of the pintle head. For the swirl gas flow case (SFR = 1.0), as the spray penetration distance is shortest, the number of discrete droplets N decreases prominently as increasing the axial position along the x -axis, leading to an increased mean Voronoi volume \bar{A} . Thus, the analysis of spray contour in the vicinity of the pintle head is the main region for SFR = 1.0. It is seen that the number of dispersed droplets is the largest and reaches a peak value at $x = 1.0$, which indicates that the swirl gas effects can promote the breakup of liquid jet or film and thereby enhance the spray characteristics. To quantitatively characterize the uniformity of dispersed droplets, the square standard deviation of Voronoi volumes is defined as $s^2 = \sum_i (A_i - \bar{A})^2 / N$ and shown in Fig. 12, where \bar{A} is the mean Voronoi volume for each slice. The results show that s^2 for the pure swirl gas flow is smallest at all slices, and s^2 for the half-swirl gas flow

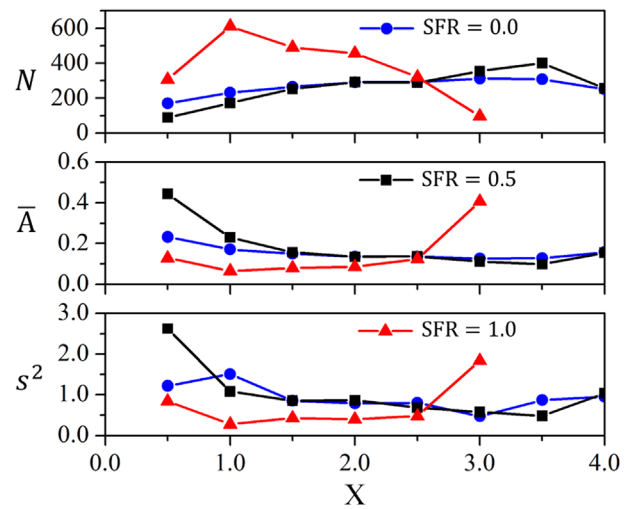


FIG. 12. Comparison of the number, mean Voronoi volume, and square deviation of Voronoi volumes at different slices along the axial direction for the representative case shown in Fig. 7 with different swirl flow ratios (SFR).

is largest at $x = 0.5$ and presents approximately the same variation trend as that for the non-swirl gas flow. An exception of s^2 for the pure swirl gas flow at $x = 3.0$ is caused by the smallest spray penetration distance and dilute spray about to end, which is, however, not opposite the discussion.

The above results of the spray characteristics might explain the combustion test in Fig. 6, since it is believed that good atomization characteristics generally produce efficient combustion. For the pure swirl gas flow, it simultaneously has the small SMD contour owing to the sufficient breakup of liquid jet or film and the uniform distribution of dispersed droplets with the smallest square deviation s^2 of Voronoi cells. Consequently, enhanced combustion performance with increased total pressure and specific impulse is achieved. Similarly, the largest square deviation s^2 for the half-swirl gas flow at $x = 0.5$ indicates the delayed breakup of liquid jet or film in the vicinity of the pintle head and non-uniform distribution of dispersed droplets, resulting in bad combustion performance with a decreased total pressure and specific impulse. This is because the droplet clustering effects characterized by Voronoi tessellation in sprays influence the flame propagation speed and the local combustion mode between the single droplet combustion and the group droplet combustion.⁷²⁻⁷⁴ The coupling effects of SMD and Voronoi distribution can benefit sub-grid modeling for the group combustion⁶⁷⁻⁶⁹ in spray combustion and merits future studies.

V. CONCLUSION

The present paper proposed a design concept for swirl-assisted spray combustion of the gas-liquid pintle injector with variable swirl intensities, aiming to solve the possible bad spray characteristics of the traditional gas-liquid injection approach due to the small spray angle and non-uniform distribution of dispersed droplets. The design concept was experimentally verified by both the cold flow test and the combustion test. The cold flow test shows that the swirl gas effects can improve the spray angle owing to the axial momentum of gas having been partially converted into the circumferential momentum. The combustion test compares three representative cases of pure non-swirl

gas flow, half-swirl gas flow, and pure swirl gas flow and shows that the swirl effects enhance the combustion performance with increased total pressure and specific impulse.

The swirl-assisted spray combustion of the gas–liquid pintle injector was also computationally investigated to explain the experimental observations. The best spray characteristics for the pure swirl gas flow are attributed to the promoted breakup of the liquid jet or film in the vicinity of the pintle head and to a broader region of dispersed droplets. The diameter and distribution of dispersed droplets are qualified by the Sauter mean diameter and the Voronoi tessellation, respectively, in which the Sauter mean diameter and Voronoi volumes show no prominent correlations but reflect two different aspects of the spray. The Sauter mean diameter contour reflects the time average of discrete droplets at a certain spatial location, whereas the Voronoi cells reflect the local characteristics of discrete droplet distribution at a certain time. The good spray characteristics tend to simultaneously have a small Sauter mean diameter but also a uniform distribution of Voronoi cells for all dispersed droplets. Thus, the swirl-assisted spray combustion in the present study can be understood as that the swirl gas effects promote the atomization of liquid jet or film, resulting in a small Sauter mean diameter and a uniform distribution of dispersed droplet qualified by the square deviation of Voronoi volumes.

The present results also consolidate the correlation between the spray characteristics of the cold flow test and the spray combustion test for the quickly predict the combustion performance. In addition, apart from the analysis of the Sauter mean diameter, the Voronoi tessellation characterizing the droplet clustering effects merits further study for its significance in the analysis of spray characteristics and the modeling of group combustion in sprays.

ACKNOWLEDGMENTS

This work was supported by National Science Foundation of China (Grant Nos. 12102437, 52176134, and U2141220), and Strategic Priority Research Program of Chinese Academy of Sciences (Grant No. XDA17030100). The work at City University of Hong Kong was partially supported by a grant from the Research Grants Council of the Hong Kong Special Administrative Region, China (Project Nos. CityU 15222421 and CityU 15218820).

AUTHOR DECLARATIONS

Conflict of Interest

The authors have no conflicts to disclose.

Author Contributions

Chengming He: Conceptualization (equal); Investigation (equal); Methodology (equal); Writing – original draft (equal). **Weihang Luo:** Data curation (equal); Investigation (equal); Methodology (equal). **Peng Zhang:** Writing – review & editing (equal). **Zhixia He:** Project administration (equal). **Lianjie Yue:** Project administration (equal); Supervision (equal).

DATA AVAILABILITY

The data that support the findings of this study are available from the corresponding author upon reasonable request.

REFERENCES

- ¹E. Betts and R. Frederick, “A historical systems study of liquid rocket engine throttling capabilities,” in *46th AIAA/ASME/SAE/ASEE Joint Propulsion Conference & Exhibit* (AIAA, 2010).
- ²M. J. Casiano, J. R. Hulka, and V. Yang, “Liquid-propellant rocket engine throttling: A comprehensive review,” *J. Propul. Power* **26**, 897–923 (2010).
- ³G. Dressler, “Summary of deep throttling rocket engines with emphasis on Apollo LMDE,” in *42nd AIAA/ASME/SAE/ASEE Joint Propulsion Conference & Exhibit* (AIAA, 2006).
- ⁴J. Yoon, S. Kim, and Y. Yoon, “Characteristics of throttleable liquid-propellant rocket injector with dual manifold: A cold flow study,” in *Proceedings of the 17th Annual Conference on Liquid Atomization and Spray Systems-Asia*, Jeju, Republic of Korea, 2010.
- ⁵Z. Dong, M. Sun, Z. Wang, J. Chen, and Z. Cai, “Survey on key techniques of rocket-based combined-cycle engine in ejector mode,” *Acta Astronaut.* **164**, 51–68 (2019).
- ⁶L. Shi, G. Zhao, Y. Yang, D. Gao, F. Qin, X. Wei, and G. He, “Research progress on ejector mode of rocket-based combined-cycle engines,” *Prog. Aerosp. Sci.* **107**, 30–62 (2019).
- ⁷W. Huang and Y. Xing, “A conceptual study of RBCC for hypersonic missile,” AIAA Paper No. 2005-4285, 2005.
- ⁸X. Wang and V. Yang, “Supercritical mixing and combustion of liquid-oxygen/kerosene bi-swirl injectors,” *J. Propul. Power* **33**, 316–322 (2017).
- ⁹J. Lux and O. Haidn, “Flame stabilization in high-pressure liquid oxygen/methane rocket engine combustion,” *J. Propul. Power* **25**, 15–23 (2009).
- ¹⁰B. L. Austin, S. Heister, and W. Anderson, “Characterization of pintle engine performance for nontoxic hypergolic bipropellants,” *J. Propul. Power* **21**, 627–635 (2005).
- ¹¹S. Jo, S. An, J. Kim, H. Yoon, and S. Kwon, “Performance characteristics of hydrogen peroxide/kerosene staged-bipropellant engine with axial fuel injector,” *J. Propul. Power* **27**, 684–691 (2011).
- ¹²N. Tiliakos, J. Tyll, R. Herdy, D. Sharp, M. Moser, and N. Smith, “Development and testing of a nitrous oxide/propane rocket engine,” AIAA Paper No. 2001-3258, 2001.
- ¹³S. Heister, “Pintle injectors,” in *Handbook of Atomization and Sprays* (Springer, 2011), pp. 647–655.
- ¹⁴M. Son, K. Radhakrishnan, J. Koo, O. C. Kwon, and H. D. Kim, “Design procedure of a movable pintle injector for liquid rocket engines,” *J. Propul. Power* **33**, 858–869 (2017).
- ¹⁵M. Son, K. Yu, J. Koo, O. C. Kwon, and J. S. Kim, “Effects of momentum ratio and weber number on spray half angles of liquid controlled pintle injector,” *J. Therm. Sci.* **24**, 37–43 (2015).
- ¹⁶P. Cheng, Q. Li, H. Chen, and Z. Kang, “Study on the dynamic response of a pressure swirl injector to ramp variation of mass flow rate,” *Acta Astronaut.* **152**, 449–457 (2018).
- ¹⁷Q.-F. Fu, L.-J. Yang, and X.-D. Wang, “Theoretical and experimental study of the dynamics of a liquid swirl injector,” *J. Propul. Power* **26**, 94–101 (2010).
- ¹⁸Z. Kang, Z.-G. Wang, Q. Li, and P. Cheng, “Review on pressure swirl injector in liquid rocket engine,” *Acta Astronaut.* **145**, 174–198 (2018).
- ¹⁹S. Kim, T. Khil, D. Kim, and Y. Yoon, “Effect of geometric parameters on the liquid film thickness and air core formation in a swirl injector,” *Meas. Sci. Technol.* **20**, 015403 (2009).
- ²⁰G. A. Vijay, N. S. V. Moorthi, and A. Manivannan, “Internal and external flow characteristics of swirl atomizers: A review,” *Atomization Sprays* **25**(2), 153–188 (2015).
- ²¹B. Ahn, M. Ismailov, and S. D. Heister, “Experimental study swirl injector dynamic response using a hydromechanical pulsator,” *J. Propul. Power* **28**, 585–595 (2012).
- ²²T. Khil, Y. Chung, V. G. Bazarov, and Y. Yoon, “Dynamic characteristics of simplex swirl injector in low frequency range,” *J. Propul. Power* **28**, 323–333 (2012).
- ²³Y. Liu, X. Chu, W. Wang, and B. Weigand, “Large-eddy simulation, convective instability, and modal causality of coaxial supersonic air–water jets considering a swirl effect,” *Phys. Fluids* **35**, 063316 (2023).
- ²⁴D. Kumar, H. S. Gaikwad, P. Kaushik, and P. K. Mondal, “Swirl driven solute mixing in narrow cylindrical channel,” *Phys. Fluids* **35**, 063604 (2023).

- ²⁵L. Zheng, R. Zhao, Y.-L. Nian, J. Liu, and W.-L. Cheng, "Numerical and experimental study of the effects of tangential to axial velocity ratio and structural parameters inside the nozzle on spray characteristics," *Phys. Fluids* **35**, 043303 (2023).
- ²⁶S. Patil and S. Sahu, "Air swirl effect on spray characteristics and droplet dispersion in a twin-jet crossflow airblast injector," *Phys. Fluids* **33**, 073314 (2021).
- ²⁷P. Cheng, Q. Li, S. Xu, and Z. Kang, "On the prediction of spray angle of liquid-liquid pintle injectors," *Acta Astronaut.* **138**, 145–151 (2017).
- ²⁸P. Cheng, Q. Li, and H. Chen, "Flow characteristics of a pintle injector element," *Acta Astronaut.* **154**, 61–66 (2019).
- ²⁹S. Lee, D. Kim, J. Koo, and Y. Yoon, "Spray characteristics of a pintle injector based on annular orifice area," *Acta Astronaut.* **167**, 201–211 (2020).
- ³⁰S. Heo, D. Hwan Kim, I. Kim, and Y. Yoon, "Effects of grooved pintle tip applied to a gas-liquid pintle injector," in *Asia-Pacific International Symposium on Aerospace Technology* (Springer, 2023).
- ³¹S. Heo, D. H. Kim, and Y. Yoon, "Effects of groove structure on spray characteristics of a throttleable pintle injector," *J. Propul. Power* **39**(9), 38–12 (2023).
- ³²S. Erazo, J. A. Day, J. Gamertsfelder, P. Khare, and J. M. Quinlan, "Pintle injector spray atomization: Liquid sheet breakup quantification," AIAA Paper No. 2021-3630, 2021.
- ³³X.-X. Fang and C.-B. Shen, "Study on atomization and combustion characteristics of LOX/methane pintle injectors," *Acta Astronaut.* **136**, 369–379 (2017).
- ³⁴F. Zhao, H. Zhang, H. Zhang, B. Bai, and L. Zhao, "Review of atomization and mixing characteristics of pintle injectors," *Acta Astronaut.* **200**, 400–419 (2022).
- ³⁵K. Sakaki, T. Funahashi, S. Nakaya, M. Tsue, R. Kanai, K. Suzuki, T. Inagawa, and T. Hiraiwa, "Longitudinal combustion instability of a pintle injector for a liquid rocket engine combustor," *Combust. Flame* **194**, 115–127 (2018).
- ³⁶L.-j. Yang, M.-h. Ge, M.-z. Zhang, Q.-f. Fu, and G.-b. Cai, "Spray characteristics of recessed gas-liquid coaxial swirl injector," *J. Propul. Power* **24**, 1332–1339 (2008).
- ³⁷H. Wu, Z. Zhang, F. Zhang, and W. L. Roberts, "Time-resolved low-pressure air-assisted spray performance and unsteadiness evaluation," *Phys. Fluids* **35**, 043335 (2023).
- ³⁸K. Khani Aminjan, M. Ghodrat, M. Heidari, A. Arjmandfard, P. Rahmanivahid, R. D. Cosme Pecho, Y. Yasin, and S. Shukhratovich Abdullaev, "Study on duplex air-blast atomizers spray in the engine real operation conditions," *Phys. Fluids* **35**, 073326 (2023).
- ³⁹K. Khani Aminjan, B. Kundu, and D. Ganji, "Study of pressure swirl atomizer with tangential input at design point and outside of design point," *Phys. Fluids* **32**, 127113 (2020).
- ⁴⁰Y. Wang, T. Yao, H. Zhao, W. Li, J. Xu, and H. Liu, "Effect of turbulence modulation caused by thread structure on coaxial air-blast atomization," *Phys. Fluids* **35**, 033302 (2023).
- ⁴¹A. Kumar and S. Sahu, "Liquid jet disintegration memory effect on downstream spray fluctuations in a coaxial twin-fluid injector," *Phys. Fluids* **32**, 073302 (2020).
- ⁴²D. Kim, M. Son, and J. Koo, "Ignition transition of coaxial kerosene/gaseous oxygen jet," *Combust. Sci. Technol.* **188**, 1799–1814 (2016).
- ⁴³W. Song, D. Shin, M. Son, and J. Koo, "Effects of nitrogen film cooling on ignition transition of gaseous oxygen/kerosene spray combustor," *Combust. Sci. Technol.* **195**(6), 1–15 (2023).
- ⁴⁴Z. Zhong, Q. Li, and Z. Wang, "Experimental research of the ignition characteristic of the gas generator with air/Lf80-01 propellant combination," in 45th AIAA/ASME/SAE/ASEE Joint Propulsion Conference & Exhibit, 2009.
- ⁴⁵X. Wang, L. Zhang, Y. Li, S.-T. Yeh, and V. Yang, "Supercritical combustion of gas-centered liquid-swirl coaxial injectors for staged-combustion engines," *Combust. Flame* **197**, 204–214 (2018).
- ⁴⁶S. Popinet, "Gerris: A tree-based adaptive solver for the incompressible Euler equations in complex geometries," *J. Comput. Phys.* **190**, 572–600 (2003).
- ⁴⁷S. Popinet, "An accurate adaptive solver for surface-tension-driven interfacial flows," *J. Comput. Phys.* **228**, 5838–5866 (2009).
- ⁴⁸S. Popinet, "Numerical models of surface tension," *Annu. Rev. Fluid Mech.* **50**, 49–75 (2018).
- ⁴⁹X. Chen, D. Ma, V. Yang, and S. Popinet, "High-fidelity simulations of impinging jet atomization," *Atomization Sprays* **23**(12), 1079–1101 (2013).
- ⁵⁰X. Yang and A. Turan, "Simulation of liquid jet atomization coupled with forced perturbation," *Phys. Fluids* **29**, 022103 (2017).
- ⁵¹D. Fuster, A. Bagué, T. Boeck, L. Le Moyne, A. Leboissetier, S. Popinet, P. Ray, R. Scardovelli, and S. Zaleski, "Simulation of primary atomization with an octree adaptive mesh refinement and VOF method," *Int. J. Multiphase Flow* **35**, 550–565 (2009).
- ⁵²G. Tomar, D. Fuster, S. Zaleski, and S. Popinet, "Multiscale simulations of primary atomization," *Comput. Fluids* **39**, 1864–1874 (2010).
- ⁵³P. Zhang and B. Wang, "Effects of elevated ambient pressure on the disintegration of impinging sheets," *Phys. Fluids* **29**, 042102 (2017).
- ⁵⁴D. Fuster, J.-P. Matas, S. Marty, S. Popinet, J. Hoepffner, A. Cartellier, and S. Zaleski, "Instability regimes in the primary breakup region of planar coflowing sheets," *J. Fluid Mech.* **736**, 150–176 (2013).
- ⁵⁵F. J. Salvador, S. Ruiz, M. Crialesi-Esposito, and I. Blanquer, "Analysis on the effects of turbulent inflow conditions on spray primary atomization in the near-field by direct numerical simulation," *Int. J. Multiphase Flow* **102**, 49–63 (2018).
- ⁵⁶J. Shinjo and A. Umemura, "Detailed simulation of primary atomization mechanisms in diesel jet sprays (isolated identification of liquid jet tip effects)," *Proc. Combust. Inst.* **33**, 2089–2097 (2011).
- ⁵⁷X. Chen and V. Yang, "Recent advances in physical understanding and quantitative prediction of impinging-jet dynamics and atomization," *Chin. J. Aeronaut.* **32**, 45–57 (2019).
- ⁵⁸H. Grosshans, R. Z. Szász, and L. Fuchs, "Development of an efficient statistical volumes of fluid-Lagrangian particle tracking coupling method," *Int. J. Numer. Methods Fluids* **74**, 898–918 (2014).
- ⁵⁹T. S. Zaripov, A. K. Gilfanov, S. M. Begg, O. Rybdylova, S. S. Sazhin, and M. R. Heikal, "The fully Lagrangian approach to the analysis of particle/droplet dynamics: Implementation into ANSYS fluent and application to gasoline sprays," *Atomization Sprays* **27**(6), 493–510 (2017).
- ⁶⁰X. Li and M. C. Soteriou, "High fidelity simulation and analysis of liquid jet atomization in a gaseous crossflow at intermediate Weber numbers," *Phys. Fluids* **28**, 082101 (2016).
- ⁶¹C. He, P. Zhang, Z. He, and L. Yue, "Analysis of spray characteristics of a jet-film injection element based on Voronoi tessellation," *Acta Astronaut.* **206**, 100–113 (2023).
- ⁶²R. A. Svehla, "Transport coefficients for the NASA Lewis chemical equilibrium program," Report No. 95N28182 (NASA Lewis Research Center, 1995).
- ⁶³B. J. McBride, "NASA Glenn coefficients for calculating thermodynamic properties of individual species," Report No. NASA/TP-2002-211556 (National Aeronautics and Space Administration, John H. Glenn Research Center, 2002).
- ⁶⁴M. Warimani, M. H. Azami, S. A. Khan, A. F. Ismail, S. Saharin, and A. K. Ariffin, "Internal flow dynamics and performance of pulse detonation engine with alternative fuels," *Energy* **237**, 121719 (2021).
- ⁶⁵N. Ashgriz, *Handbook of Atomization and Sprays: Theory and Applications* (Springer Science & Business Media, 2011).
- ⁶⁶H. Wu, F. Zhang, and Z. Zhang, "Droplet breakup and coalescence of an internal-mixing twin-fluid spray," *Phys. Fluids* **33**, 013317 (2021).
- ⁶⁷V. Boddapati, M. Manish, and S. Sahu, "A novel approach for conditional measurement of droplet size distribution within droplet clusters in sprays," *Exp. Fluids* **61**, 42 (2020).
- ⁶⁸M. Manish and S. Sahu, "Optical characterization of droplet clusters and group combustion in spray diffusion flames," *Proc. Combust. Inst.* **38**, 3409–3416 (2021).
- ⁶⁹S. Sahu, "Analysis of droplet clustering in air-assist sprays using Voronoi tessellations," *Phys. Fluids* **30**, 123305 (2018).
- ⁷⁰F. Aurenhammer, "Voronoi diagrams—A survey of a fundamental geometric data structure," *ACM Comput. Surv.* **23**, 345–405 (1991).
- ⁷¹L. Mu, "Polygon characterization with the multiplicatively weighted Voronoi diagram," *Prof. Geogr.* **56**, 223–239 (2004).
- ⁷²J. Urzay, "A revised spray-combustion diagram of diffusion-controlled burning regimes in fuel-spray clouds," in *Annual Research Briefs 2011* (Center for Turbulence Research, Stanford, CA, 2011), pp. 193–198, see https://web.stanford.edu/group/ctr/ResBriefs/2011/17_urzay.pdf.
- ⁷³H. Chiu, R. Ahluwalia, and E. Croke, "Spray group combustion," in *16th Aerospace Sciences Meeting* (AIAA, 1978).
- ⁷⁴H. Chiu and T. Liu, "Group combustion of liquid droplets," *Combust. Sci. Technol.* **17**, 127–142 (1977).